

## FDTD Modeling of Coils for Wireless Charging Applications

Santosh Pokhrel<sup>1</sup>, Gregory Moss<sup>2</sup>, and Jamesina J. Simpson<sup>1</sup>

<sup>1</sup> Department of Electrical Engineering  
University of Utah, Salt Lake City, UT, 84112, USA  
santoshpokhrel1991@gmail.com, jamesina.simpson@utah.edu

<sup>2</sup> Remcom, State College, PA, 16801, USA  
gregory.moss@remcom.com

**Abstract** — Wireless power transfer using inductive/resonant coupling is studied using the finite-difference time-domain (FDTD) method. Three-dimensional FDTD models are used to simulate the source and load loops as well as frequency-dependent magnetized ferrite shields. A series of tests are run to determine the required distance between the coils and the domain edges, the PML thickness, and convergence level. The FDTD-calculated coil parameters (self-inductance and quality factor) are then validated against measurement results. The efficiency of the inductive link is studied without ferrite shields and then with two ferrite slabs added. It is observed that adding ferrite slabs improves the efficiency by ~40%.

**Index Terms** — Coils, FDTD, flux coupling, magnetized ferrite, simulation and wireless charging.

### I. INTRODUCTION

Interest in wireless power transfer has been growing due to its utility and convenience when applied to numerous applications [1], including charging of laptops to mobile phones, medical implants [2], near field communication (NFC) antennas [3], and electric vehicles [4]. Generally, low frequencies (kHz and MHz frequencies) are used for wireless charging applications due to safety issues [5]. For instance, according to the Qi wireless charging standard [6], wireless charging of mobile phones is performed in the lower kHz band (110 kHz – 205 kHz). Wireless charging for biological telemetry [7] is performed in the lower MHz frequency band.

To transmit power wirelessly between transmitter and receiver coils, non-radiative techniques [2], [8]-[11] are typically used, such as inductive coupling [10] and magnetic resonant coupling [11]. As shown in Fig. 1, a source coil (loop) connected to an AC power source generates magnetic flux. When a load loop is brought into the vicinity of the source loop, an electromotive force is induced in the load coil which eventually drives current through it. The performance of the coupling is

dependent on its power transfer efficiency (PTE) and power transmission distance. The PTE can be improved by shielding the coils with magnetized ferrite slabs. Another possibility is to use metamaterials [12].

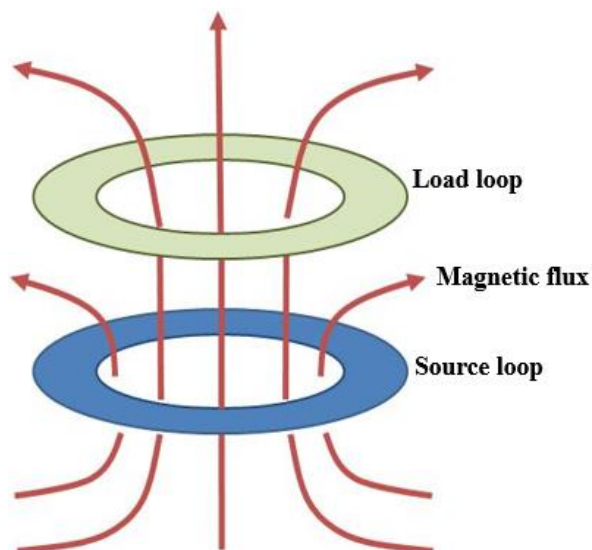


Fig. 1. Magnetic flux coupling between a source and load loop.

Various commercial electromagnetic (EM) solvers exist that may be used to simulate coils. For example, the frequency domain solver [13], [14] provided by ANSYS may be used, as well as the magnetostatic domain solver [15] provided by Computer Simulation Technology (CST). Further, the finite-difference time-domain (FDTD) has been used to model RF coils for different applications, such as magnetic resonant imaging (MRI) [16], biomedical telemetry system [17], open vertical field magnetic resonance guided focused ultrasound system [18], nuclear magnetic resonance (NMR) [19], inductive power transfer system [20] etc. Similarly, using the FEKO electromagnetics software, the Method

of Moments (MOM) has been applied to wireless power transfer via magnetic resonance coupling [21].

An advantage of FDTD for this application is that it can be used to simulate anisotropic and frequency-dependent materials such as magnetized ferrite and magnetized plasma in a relatively easier manner (e.g., [22]). In this paper, XFDTD [23] is used to simulate wireless charging coil designs with magnetized ferrite shields.

There are a number of challenges when simulating low frequency wireless charging coils using the FDTD method. First, the dimensions of the coils are extremely small, on the order of millimeters. As a result, a large number of grid cells (high resolution mesh) are required to correctly resolve the coil geometry. This is especially important because the fundamental coil parameters (inductance and AC resistance) are extremely sensitive to the coil dimensions, therefore a high degree of spatial accuracy is required. Second, the rate of convergence can be extremely slow for low frequency problems. Third, thick absorbing boundary conditions (such as a perfectly matched layer (PML)) [24] are needed to effectively absorb low frequency waves, which have long wavelengths compared to the dimensions of the grid cells.

We note that an inductive power system using two-step scaled frequency FDTD methods has been recently reported [20]. However, the effect of the magnetized ferrite on the important coil parameters such as self-inductance, quality factor, mutual inductance, coupling coefficient and efficiency was not quantified. Therefore, the contribution of this paper includes: (1) comparing simulation results with measurements; and (2) using the FDTD method to perform a complete 3-D simulation of two coils while including magnetized ferrite shields. In particular, the effect of the magnetized ferrite on the important coil parameters is computed. These simulation results provide additional insight into designing wireless charging coil systems.

This paper is organized as follows: In Section II, an equivalent circuit model of the coil system is provided. Section III elaborates on the challenges of using FDTD for this application. Information is also provided for setting up effective simulations. In addition, FDTD-calculated results are validated against measurements. Section IV provides details on magnetized ferrite and the results including it in the FDTD simulations. Finally, Section V discusses strategies for boosting the magnetic flux coupling between coils.

## II. EQUIVALENT CIRCUIT MODEL

The fundamental structure for wireless power transfer consists of two coils: a transmitter (driver) coil connected to an AC excitation and a receiver (load) coil (as shown in Figs. 1 and 2). An equivalent circuit is shown in Fig. 3.

The two coils may be represented by a two-port network with the transmitter coil attached to Port-1 and the receiver coil attached to Port-2. The two-port network results in a  $2 \times 2$  S-parameter matrix, which are evaluated at the nodes during the simulation. The measured S-parameters are obtained from the terminals (see Fig. 2). In the measurements, the S-parameters are obtained from the vector network analyzer (VNA). The S-parameters are then converted into impedances ( $Z$ ). The self-inductances ( $L_1$  and  $L_2$ ) of the transmitter coil and the receiver coil, respectively are determined by dividing the imaginary part of  $Z_{11}$  and  $Z_{22}$ , respectively, by the angular frequency. The real part of  $Z_{11}$  yields the parasitic resistance of the coil.  $R_1$  and  $R_2$  are the parasitic resistances of the two coils. The mutual inductance ( $M$ ) is determined by dividing the imaginary component of  $Z_{12}$  or  $Z_{21}$  by the angular frequency. Two capacitors ( $C_1$  and  $C_2$ ) may be connected in series to represent the resonant circuit at the desired frequency.

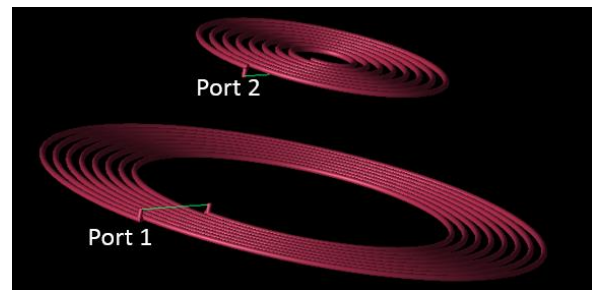


Fig. 2. Inductive link (driver coil and load coil) modeled in XFDTD. The bigger coil at bottom is the transmitter coil, and the smaller one at the top is the receiver coil. The green line in the driver coil represents the resistive voltage connection between two terminals. Similarly, the green line in the load coil represents the resistive load connection between two terminals.

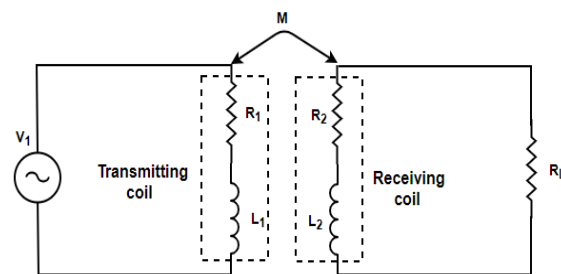


Fig. 3. Circuit model of the two port network representing the two coils.

$Q_1$  is the intrinsic quality factor of the transmitting coil,  $Q_2$  is the intrinsic quality factor of the receiving coil, and  $Q_2L$  is the loaded quality factor of the receiving coil. The quality factors are determined using equations (1) – (3):

$$Q_1 = \frac{\omega L_1}{R_1}, \quad (1)$$

$$Q_2 = \frac{\omega L_2}{R_2}, \quad (2)$$

$$Q_{2L} = \frac{\omega L_2}{R_2 + R_L}. \quad (3)$$

$K_{12}$  is the coupling coefficient representing the magnetic flux coupling between the two coils (the transmitter and receiver coils). Its value depends on the mutual inductance between the coils, and the self-inductance of the individual coils, as shown in (4). Numerically, its value ranges from 0 to 1. A value of zero indicates that little or no coupling is achieved, and a value of one indicates that perfect coupling is achieved. Practically, it is impossible to achieve perfect coupling:

$$K_{12} = \frac{M}{\sqrt{L_1 L_2}}. \quad (4)$$

The power transfer efficiency (PTE) of the link determines how much total power has been coupled to the receiver. Its value gives the final figure of merit of the system. The PTE depends on the magnetic flux coupling between the coils, the quality factors of both coils, and the resistance of the load and receiver coils. The expression for the PTE is given by (5):

$$PTE = \frac{K_{12}^2 Q_1 Q_{2L}}{1 + K_{12}^2 Q_1 Q_{2L}} \cdot \frac{R_L}{R_L + R_2}. \quad (5)$$

Equations (1-5) are used in the upcoming sections analyze the system.

### III. VALIDATION

#### A. Simulation details

The simulation examples provided here are for the kHz range, however, an analogous procedure may be followed for higher frequencies. An example circular coil is modeled with a diameter of 67 mm, 10 turns, 1 mm spacing between turns, and a 0.8 mm wire diameter. The two ends of the coil are connected via a copper wire with a resistive voltage source having an internal resistance of 50 ohms. A Gaussian source time-waveform is used to excite a range of frequencies from DC to 260 kHz. A conductivity of  $5.95 \times 10^7$  S/m is used for the copper.

The models employ conformal meshing, [25] which helps to resolve the complex geometry and small gap efficiently. The spatial grid resolution is 0.4 mm. At this resolution, two to three cells are used to resolve the traces of the conductor and one to two cells are used to resolve the gap between the turns of the coil. Additional simulations demonstrated that doubling the number of cells used to model the wire and gap (i.e., doubling the grid resolution) does not change the results significantly (for both cases, the results compare well with theory and measurements as shown in Section III B). We note that advanced computational techniques have been developed to more accurately and efficiently model thin wires in FDTD models (e.g., [26]-[27]). However,

XFDTD, which was used in the simulations does not provide this modeling capability in its software.

By default, XFDTD uses a tenth of a wavelength free space padding between the object and the grid boundaries. However, at the low frequencies of interest here, a one-tenth wavelength padding would increase the simulation size by around 500,000 grid cells on each direction. By running a series of tests and comparing against measurements, it is found that the simulation domain may be twice the largest dimension of the coil. As a result, a grid with  $335 \times 335 \times 40$  cells in the x-, y-, and z-directions, respectively, is used to model the coil.

The small grid cell dimensions relative to the wavelength at low frequencies also influences the implementation and performance of absorbing boundary conditions. A convolutional PML (CPML) [28] is implemented along all of the edges of the grid. In Fig. 4, the relative error (reflection error) caused by the PML is compared for different PML thicknesses (10 cells, 15 cells and 20 cells). A 20-cell thick PML (black plot in Fig. 2) has less than 1% error. Appendix A summarizes the PML parameters that are used in the simulation. It may be possible to tweak these parameters to improve the PML absorption. Additionally, using an even thicker PML than 20 cells is expected to further reduce the error. However, a thicker PML requires more grid cells and thus increases the memory and computational time of the simulation. Therefore, if thicker PMLs are employed, a level of error must be chosen that makes a suitable trade-off between numerical accuracy and the simulation time.

A time step set to the Courant limit [29] is used. The complete simulation is run on eight graphics processing units (GPUs).

As for many commercial solvers, before simulation begins, an acceptable level of a numerical convergence must be chosen (as time-stepping progresses). For example, the electric or magnetic field components between two successive time-step iterations should not change by a value of more than 0.01 or 20 dB, i.e.,  $|x_n - x_{n-1}| < 0.01$ , where  $x$  is an electric or magnetic field component at one position within the grid. It is desirable to have the convergence level as low as possible to yield higher accuracy. Higher accuracy (low convergence level) is obtained by running longer simulations with a smaller threshold of electric or magnetic field variations between time steps (such as 0.001 or even smaller). This ensures that the (pulsed) source decays fully to zero. Otherwise, undesirable frequency components (out of the band) will appear in the spectrum. However, there is a sluggish rate of convergence (global order of accuracy) at low frequencies in the numerical EM solution. Figure 5 plots frequency vs. the imaginary part of coil impedance for different convergence levels.

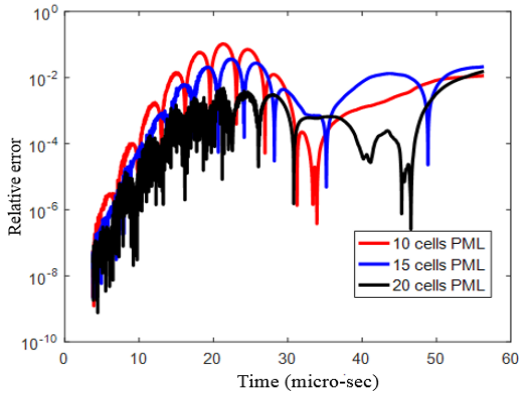


Fig. 4. Relative error (reflection error) for different PML thicknesses.

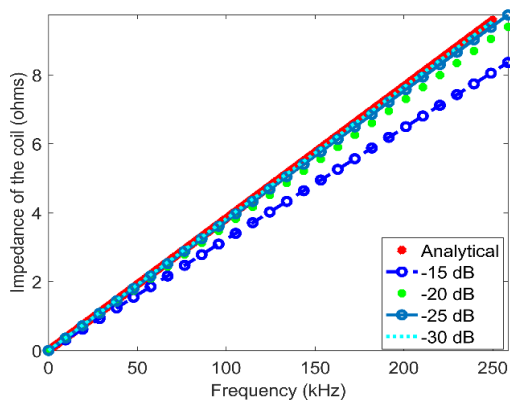


Fig. 5. Comparison of different levels of convergence with analytical impedance (imaginary part) of the coil as simplified by Wheeler approximation.

Table 1 lists the simulation time and error level corresponding to each convergence level (compared to the analytical result). From Table 1, a convergence level of -25 dB yields an error of less than 2%. The numerical solution converges to an analytical solution with an error around 0.3% for a convergence of -30 dB. Using a better convergence level than -30 dB will minimize the error, however the simulation time increases significantly. The simulation time nearly doubles when changing from a convergence level of -25 dB to -30 dB.

Table 1: Comparison of simulation time with different convergence level

Level of Convergence (in dB)	Time of Simulation (in Hours)	Error (at 156 kHz)
-15	0.55	17.28%
-20	1.1	5.44%
-25	1.46	1.8%
-30	2.85	0.3%

All of the remaining simulations are performed at a convergence level of -30 dB.

**B. Comparison**

The self-inductance of the coil depends on the diameter of the wire, number of turns, spacing between the turns, inner diameter, outer diameter of coil, and permeability of the core [30]. The quality factor of the coil depends on its self-inductance and parasitic resistance (see (1)-(3)).

The self-inductance of the transmitter and receiver coils are calculated via FDTD and compared with both measurement results (as given in [31]) and approximate analytical values as calculated by the Wheeler expression for planar spiral coils [13]. Figure 6 shows the laboratory transmitter and receiver coils used in the measurements. The coil measurements were performed in [31] using a vector network analyzer (VNA). The dimensions of the two coils are tabulated in Table 2.

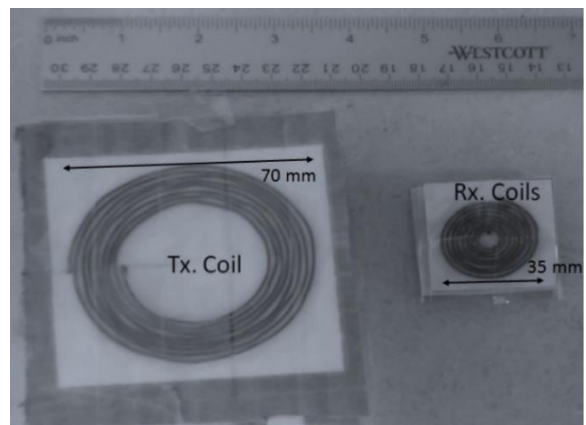


Fig. 6. Coil used for measurement in lab (figure courtesy of [31]). The left coil is the transmitter coil and the right coil is the receiver coil.

Table 2: Dimension for both transmitter and receiver coils

Coil	Diameter (mm)	Number of Turns	Wire Radius (mm)	Gap (mm)
<b>Transmitter</b>	70	8	0.4059	1
<b>Receiver</b>	35	8	0.4059	1

The FDTD grid is run at a resolution of 0.4 mm and at the Courant time-stepping limit. A resistive voltage source with an internal resistance of 50 ohms is modeled on a single electric field component.

Table 3 compares the inductance of both the transmitter and receiver coils. The FDTD simulated inductance values are very close to the measured and analytical values. The error in both cases is less than 2%.

Table 4 compares the simulated and measured quality factor. The simulated quality factor is evaluated using (1) and (2). The quality factor is very sensitive to the coil's inductance and parasitic resistance. There is no standard way to analytically determine the parasitic resistance of the coil [32] (unlike Wheeler's method for calculating self-inductance), so Table 4 does not include analytical results.

Table 3: Comparison of self-inductance of the coil at 5 MHz

	Self-Inductance ( $\mu H$ ) of Transmitter Coil	Self-Inductance ( $\mu H$ ) of Receiver Coil
<b>Analytical (Wheeler Approximation)</b>	5.088	1.097
<b>Measurement</b>	5	1
<b>FDTD Simulation</b>	5.0038	1.01

Table 4: Comparison of quality factor of the coil at 5 MHz

Methods	Transmitter Coil	Receiver Coil
<b>Measurement</b>	150.00	70.00
<b>FDTD Simulation</b>	256.02	157.07

The measured and simulated results in Table 4 are not in good agreement. A likely reason for the discrepancy is that the FDTD simulation does not account for some physical resistances present in the measured circuit, specifically the stray resistance of the VNA cables/clippers. As a sanity check, the same coils are modeled in another electromagnetic solver (CST) and quality factors of 304 and 176 are obtained for the transmitting and receiving coils, respectively. These values are also too high compared with the measurements result. We conclude that the simulations are missing the physical resistances caused by the VNA cables / clippers during the measurement.

To emulate the parasitic resistances of the physical coils, an external resistance of 0.43 ohms and 0.24 ohms are added in series with the transmitter and receiver coils, respectively. These external resistances are obtained by calculating what additional resistances in the FDTD simulation would lead to quality factors that more closely match the measured quality factors of the coils (these values are shown in Table 5). Note that the inaccuracy in the quality factors caused by the missing external resistances in the measurement do not influence the magnetic flux generated by the coil or the effect of the ferrite shields on the inductance and coupling coefficient, which will be studied next.

Table 5: Comparison of the adjusted Q of the coils at 5 MHz

Methods	Transmitter Coil	Receiver Coil
<b>Measurement</b>	150	70
<b>FDTD Simulation</b>	150.57	71.7

#### IV. EFFECT OF MAGNETIZED FERRITE

Ferrite is an anisotropic, dispersive and gyrotropic magnetic material [33] with a magnetic permeability characterized by (6) [34]:

$$\mu = \mu_o \begin{bmatrix} 1 + \chi_m(\omega) & -jk(\omega) & 0 \\ jk(\omega) & 1 + \chi_m(\omega) & 0 \\ 0 & 0 & 1 \end{bmatrix}, \quad (6)$$

where the susceptibilities are given by (7) and (8).

$$\chi_m(\omega) = \frac{(\omega_o + j\omega\alpha)\omega_m}{(\omega_o + j\omega\alpha)^2 - \omega^2}, \quad (7)$$

$$k(\omega) = \frac{-\omega\omega_m}{(\omega_o + j\omega\alpha)^2 - \omega^2}, \quad (8)$$

$$\omega_o = \gamma_m H_o, \quad (9)$$

$$\omega_m = \gamma_m 4\pi M_o. \quad (10)$$

Note:  $\alpha$ ,  $\gamma_m$ ,  $H_o$  and  $4\pi M_o$  refer to the damping constant, gyromagnetic ratio, static biasing field and static magnetization, respectively, of a ferrite. Usually, ferrite materials are represented by the empirical formula  $XO \cdot Fe_2O_3$  where 'X' can be any divalent metal (such as cobalt, manganese, nickel, zinc) [34].

The FDTD implementation of a magnetized ferrite involves special updates for the tangential magnetic field components ( $H_x$  and  $H_y$ ). The stability of the update equations depends on the damping constant ( $\alpha$ ). Note that the FDTD calculation of EM propagation in ferrite materials has been successfully validated against exact solutions in the past (e.g., [35], [36]).

The presence of a ferrite alters the intensity of the magnetic field. It acts as a magnetic shield and boosts the inductance of the coil, thereby improving the magnetic flux coupling between the links. Therefore, adding a ferrite shield can help to increase the PTE of a wireless power transfer system. Parameters extracted from a datasheet for the magnetized ferrite used in the following simulations and measurements are shown in Table 6. This data is from the datasheet for the ferrite plate RP series from Laird Smart Technology. The magnetic loss tangent ( $\tan \delta$ ), which is defined as the ratio of imaginary permeability to real permeability, is 0.04 for the ferrite material specified in Table 6.

The simulation case of Section III is now modeled with two ferrite slabs added (behind each coil). The dimensions of the ferrite slabs (length and width) are slightly larger than the dimensions of the coils. The ferrite slab that is used near the transmitter coil is 80 mm  $\times$  80 mm  $\times$  5 mm, whereas the ferrite slab that

is used near the receiver coil is  $40 \text{ mm} \times 40 \text{ mm} \times 5 \text{ mm}$ . The slabs are finely meshed in the lengthwise directions at the spatial resolution used for the coils (0.4 mm). The thickness of the slabs are resolved using 0.8 mm resolution.

Table 6: Datasheet specification of magnetized ferrite (RP Series) as provided by Laird

Property	Value
Real permeability	250
Imaginary permeability	10
Flux density	390 mT
Field strength	1200 A/m
Resistivity	$10^7 \text{ ohm-cm}$

Figure 7 shows the magnetic flux when no ferrite shields are used. The magnetic flux extends away from the transmitter coil on both sides. On the other hand, Fig. 8 shows how the magnetic flux is confined to the space between the two coils after the magnetized ferrite shields (represented by the red lines) have been added. Depending upon the application at hand, a ferrite shield may be added next to the transmitter coil (as for a biological telemetry system) or added next to both coils (as for wireless charging of mobile phones). Note that a minimum distance ( $\sim \text{mm}$ ) should be maintained between the coil traces and the ferrite to avoid an electrical contact between them [10].

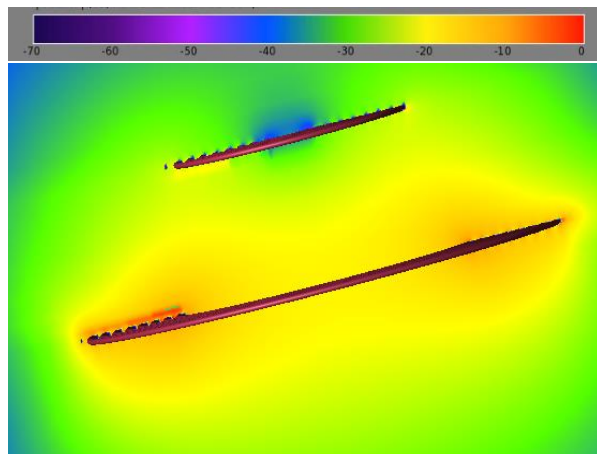


Fig. 7. Magnetic field over a 2-D cross-sectional slice through the center of the coils for the case without the ferrite slabs. The coils (driver and load) are separated by a distance of 20 mm. The colorbar represents the value of the absolute magnetic field using a dB scale.

Comparing Figs. 7 and 8, it is observed that the self-inductance of the coil improves after adding the ferrite slabs as current finds additional dispersive and resistive paths along which to flow. The addition of the ferrite slabs also increases the effective parasitic resistance of

the coil. It is difficult to quantify how ferrite, a frequency dependent gyrotropic medium, changes the parasitic components.

Figure 9 compares the FDTD-calculated quality factor of the receiver coil with and without magnetized ferrite. The quality factor is seen to decrease by around 30%. This is due to the parasitic components (especially resistance) changing after the ferrite slabs are added next to the coils.

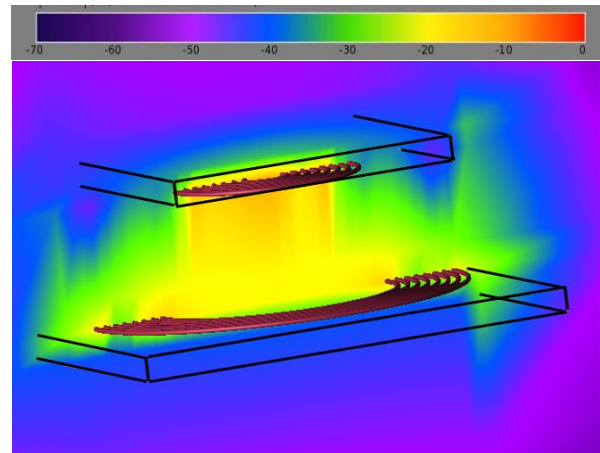


Fig. 8. Magnetic field confined between the coils after adding two ferrite slabs of thickness 5 mm. The black boxes outline the two ferrite slabs. The colorbar represents the value of the absolute magnetic field using a dB scale.

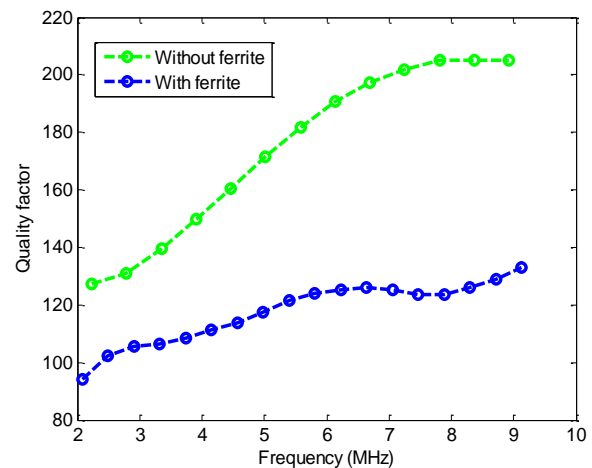


Fig. 9. Comparison of the quality factor of the receiver coil before and after the ferrite slabs are added.

As can be seen in (5), the PTE is directly proportional to  $K_{12}^2 Q_1 Q_{2L}$ . According to Fig. 10, the  $K_{12}^2$  increases by  $\sim 60\%$  when the ferrite slabs are included. This is because the mutual inductance increases when the flux on one side of the coil is shielded.

Figure 11 shows that the mutual inductance almost doubles with the addition of the ferrite shields. At 5 MHz, it increased from 0.275  $\mu H$  to 0.55  $\mu H$ . Although the quality factor decreases when ferrite is added (as shown in Fig. 9), the PTE improves slightly with the ferrite shields because the  $K_{12}^2$  term (which depends on mutual inductance) changes more dramatically than the quality factor (which depends on self-inductance).

As shown in Fig. 12, the PTE at 5 MHz is improved by ~40% because of the ferrite shields. The improvement would likely be less when a ferrite shield is used only on one side of one coil, rather than on the sides of both coils as shown in Fig. 8.

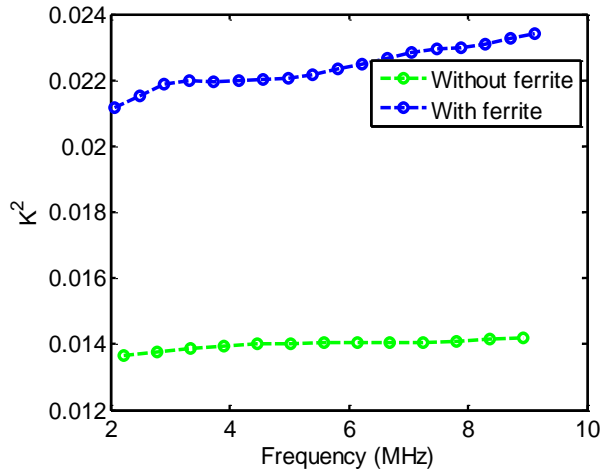


Fig. 10. Comparison of  $K_{12}^2$  for the receiver coil before and after the ferrite slabs are added. The Y-axis is expressed in decimal (not in percentage).

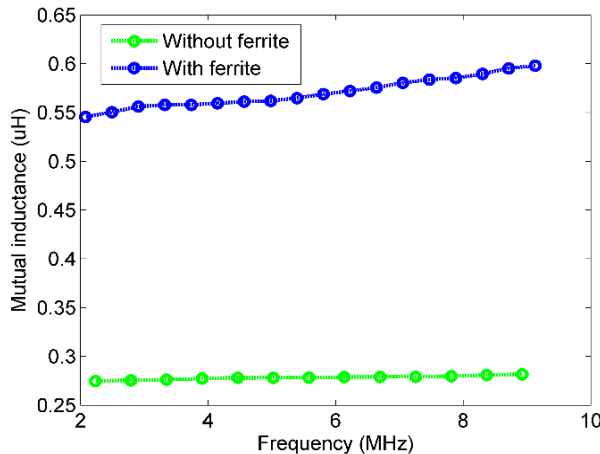


Fig. 11. Comparison of the mutual inductance before and after the ferrite slabs are added.

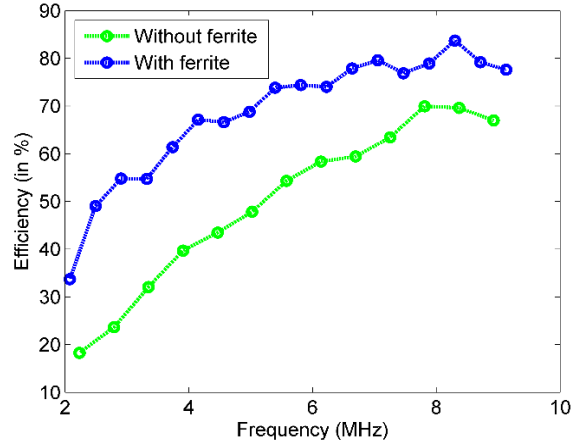


Fig. 12. Comparison of the PTE before and after the ferrite slabs are added.

### V. TECHNIQUES FOR IMPROVING PTE

The parasitic components (especially resistance) are the major impediment to achieving a high PTE. The AC parasitic resistance in the coil is caused primarily by eddy current loss and proximity effect. The former effect is caused by changing magnetic field in the conductor, and the latter effect is the phenomena of current crowding in the conductor when AC current is passed through the coils with multiple nearby conductors. These effects may be minimized by using Litz wire. Litz wire has many insulated thin strands, which can considerably reduce the skin effect and proximity effect. However, modeling many thin strands of Litz wire in place of one thicker copper wire would greatly increase the computational requirements (memory and simulation time).

Additionally, the magnetic field enhancement is dependent on the dimensions of the ferrite slab and its placement. The larger the piece of ferrite, the more the flux is shielded. However, using a larger piece of ferrite takes up more space and this can be a concern for industrial applications. Then, an optimal distance between the coil and ferrite slab must be determined for real applications. Ideally, there would be no separation between the coils and ferrite slabs, but this is infeasible because any electrical contact between them should be avoided [10].

Finally, multiple coils (instead of just two coils) may be used to further boost the flux coupling [7], [37]. Instead of direct coupling between a driver and load, the driver can couple the flux to a transmitter, the transmitter to a receiver, and then finally the receiver to a load. The transmitter and receiver should resonate at the same frequency for maximum flux coupling.

## VI. CONCLUSION

Wireless power transfer was modeled using the FDTD method. First, two spiral inductive coils were modeled with open boundaries. The simulated values were validated against measurement results. Then the effect of adding magnetized ferrite slabs was studied. It was found that the quality factor of the coils slightly decreased with the addition of the ferrite slabs. However, there was an appreciable boost in mutual inductance and flux coupling between the coils after the ferrite slabs were added. As a result, the PTE improved by ~40%. For the coil dimensions given in Table 1, a maximum PTE of 85% was achieved for a two coil system separated by 20 mm.

A two-coil design is efficient for wireless power transmission for biological implants. A three-coil system [7] or multiple coils may be used to further enhance the efficiency of the coil system. There are additional constraints for biomedical applications such as electromagnetic safety standards, biocompatible, longevity requirements [38], [39] etc.

FDTD is an effective method for modeling coil geometries and magnetized ferrite slabs. Due to the required small spatial resolution of the grid to resolve the coil geometry and spacing, and because of the ferrite specifications, the numerical time step may be very small in order to maintain stability. However, the computation may be distributed onto a supercomputing cluster in a straight-forward manner and use parallel I/O such as hierarchical data format (HDF) [40] for efficient processing.

## APPENDIX

The PML parameters that are used in the simulations are listed below. Note that the parameters are scaled tensor parameters, and they carry the same meaning as used in [29]. The  $x$ ,  $y$  and  $z$  subscripts refer to the spatial coordinate axes:

$$\begin{aligned} a_x^{max} &= 0, a_y^{max} = 0, a_z^{max} = 0, \\ \kappa_x^{max} &= 1, \kappa_y^{max} = 1, \kappa_z^{max} = 1, \\ m &= 4, ma = 2. \end{aligned}$$

These PML parameters are equivalent to UPML. The XFDTD software uses UPML parameters by default.

## ACKNOWLEDGEMENT

The authors would like to thank Remcom (Electromagnetic Simulation Software and EM Modeling) company for access to XFDTD software and supercomputing resources.

## REFERENCES

- [1] K. Wu, D. Choudhury, and H. Matsumoto, "Wireless power transmission, technology, and applications," *Proc. IEEE*, vol. 101, no. 6, pp. 1271-1275, 2013.
- [2] R. Bashirullah, "Wireless implants," *IEEE Microw. Mag.*, vol. 11, no. 7, pp. S14-S23, 2010.
- [3] K. Finkenzeller, *RFID Handbook: Fundamentals and Applications in Contactless Smart Cards, Radio Frequency Identification and Near-Field Communication*. John Wiley & Sons, 2010.
- [4] F. Musavi and W. Eberle, "Overview of wireless power transfer technologies for electric vehicle battery charging," *IET Power Electron.*, vol. 7, no. 1, pp. 60-66, 2014.
- [5] O. P. Gandhi, "Electromagnetic fields: Human safety issues," *Annu. Rev. Biomed. Eng.*, vol. 4, no. 1, pp. 211-234, 2002.
- [6] G. Kiruthiga, M. Y. Jayant, and A. Sharmila, "Wireless charging for low power applications using Qi standard," in *Communication and Signal Processing (ICCSP), 2016 International Conference on*, pp. 1180-1184, 2016.
- [7] A. K. RamRakhyani and G. Lazzi, "On the design of efficient multi-coil telemetry system for biomedical implants," *IEEE Trans. Biomed. Circuits Syst.*, vol. 7, no. 1, pp. 11-23, 2013.
- [8] S. Y. R. Hui, W. Zhong, and C. K. Lee, "A critical review of recent progress in mid-range wireless power transfer," *IEEE Trans. Power Electron.*, vol. 29, no. 9, pp. 4500-4511, 2014.
- [9] J. D. Joannopoulos, A. Karalis, and M. Soljacic, "Wireless non-radiative energy transfer," June 2010.
- [10] G. Vigneau, M. Cheikh, R. Benbouhout, and A. Takacs, "Design and modeling of PCB coils for inductive power charging," *Wirel. Power Transf.*, vol. 2, no. 2, pp. 143-152, 2015.
- [11] A. Kurs, A. Karalis, R. Moffatt, J. D. Joannopoulos, P. Fisher, and M. Soljacic, "Wireless power transfer via strongly coupled magnetic resonances," *Science*, vol. 317, no. 5834, pp. 83-86, 2007.
- [12] J. Chen and H. Tan, "Metamaterial for wireless power transfer system at 13.56 MHz with coil misalignment," in *Microwave, Antenna, Propagation, and EMC Technologies (MAPE), 2017 7th IEEE International Symposium on*, pp. 313-317, 2017.
- [13] A. C. Polycarpou, "Introduction to the finite element method in electromagnetics," *Synth. Lect. Comput. Electromagn.*, vol. 1, no. 1, pp. 1-126, 2005.
- [14] Q. Yu and T. W. Holmes, "A study on stray capacitance modeling of inductors by using the finite element method," *IEEE Trans. Electromagn. Compat.*, vol. 43, no. 1, pp. 88-93, 2001.
- [15] M. Studio, "Cst-computer simulation technology," *Bad. Nuheimer. Str.*, vol. 19, p. 64289, 2008.
- [16] D. M. Sullivan and J. Nadobny, "FDTD simulation of RF coils for MRI," in *Antennas and Propagation Society International Symposium, 2009, APSURSI'09*,

- IEEE*, 2009, pp. 1-4.
- [17] S. Schmidt and G. Lazzi, "Use of the FDTD thin-strut formalism for biomedical telemetry coil designs," *IEEE Trans. Microw. Theory Tech.*, vol. 52, no. 8, pp. 1952-1956, 2004.
- [18] X. Xin, D. Wang, J. Han, Y. Feng, Q. Feng, and W. Chen, "Numerical optimization of intra-operative RF coil for open vertical-field MRgFUS using hybrid MoM/FDTD method," in *Biomedical Imaging: From Nano to Macro, 2011 IEEE International Symposium on*, 2011, pp. 750-753.
- [19] M. Gupta and P. Agarwal, "To model magnetic field of RF planar coil for portable NMR applications," in *Inventive Computing and Informatics (ICICI), International Conference on*, 2017, pp. 490-494.
- [20] M. Zang, M. Clemens, C. Cimala, J. Streckert, and B. Schmuelling, "Simulation of inductive power transfer systems exposing a human body with two-step scaled-frequency FDTD methods," *IEEE Trans. Magn.*, vol. 53, no. 6, pp. 1-4, June 2017.
- [21] X. Shi, C. Qi, M. Qu, S. Ye, and G. Wang, "Effects of coil locations on wireless power transfer via magnetic resonance coupling," *Appl. Comput. Electromagn. Soc. J.*, vol. 31, no. 3, pp. 270-278, 2016.
- [22] S. Pokhrel, V. Shankar, and J. J. Simpson, "3-D FDTD modeling of electromagnetic wave propagation in magnetized plasma requiring singular updates to the current density equation," *IEEE Trans. Antennas Propag.*, vol. 66, no. 9, pp. 4772-4781, 2018.
- [23] R. XFDTD, *Electromagnetic Solver Based on the Finite Difference Time Domain Method*. Remcom Inc., 2005.
- [24] J.-P. Bérenger, "Perfectly matched layer (PML) for computational electromagnetics," *Synth. Lect. Comput. Electromagn.*, vol. 2, no. 1, pp. 1-117, 2007.
- [25] G. Waldschmidt and A. Taflove, "Three-dimensional CAD-based mesh generator for the Dey-Mitra conformal FDTD algorithm," *IEEE Trans. Antennas Propag.*, vol. 52, no. 7, pp. 1658-1664, 2004.
- [26] R. M. Makinen, J. S. Juntunen, and M. A. Kivikoski, "An improved thin-wire model for FDTD," *IEEE Trans. Microw. Theory Tech.*, vol. 50, no. 5, pp. 1245-1255, 2002.
- [27] M. Douglas, M. Okoniewski, and M. A. Stuchly, "Accurate modeling of thin wires in the FDTD method," in *IEEE Antennas and Propagation Society International Symposium. 1998 Digest. Antennas: Gateways to the Global Network. Held in conjunction with: USNC/URSI National Radio Science Meeting (Cat. No. 98CH36)*, 1998, vol. 2, pp. 1246-1249.
- [28] J. A. Roden and S. D. Gedney, "Convolution PML (CPML): An efficient FDTD implementation of the CFS-PML for arbitrary media," *Microw. Opt. Technol. Lett.*, vol. 27, no. 5, pp. 334-339, 2000.
- [29] A. Taflove, S. C. Hagness, and M. Picket-May, "Computational electromagnetics: The finite-difference time-domain method," in *The Electrical Engineering Handbook*, Elsevier Inc., 2005.
- [30] S. S. Mohan, M. del Mar Hershenson, S. P. Boyd, and T. H. Lee, "Simple accurate expressions for planar spiral inductances," *IEEE J. Solid-State Circuits*, vol. 34, no. 10, pp. 1419-1424, 1999.
- [31] M. Machnoor, E. S. G. Rodríguez, P. Kosta, J. Stang, and G. Lazzi, "Analysis and design of a 3-coil wireless power transmission system for biomedical applications," *IEEE Trans. Antennas Propag.*, 2018.
- [32] C. Peters and Y. Manoli, "Inductance calculation of planar multi-layer and multi-wire coils: An analytical approach," *Sens. Actuators Phys.*, vol. 145, pp. 394-404, 2008.
- [33] B. Lax and K. J. Button, "Microwave ferrites and ferrimagnetics," 1962.
- [34] K. S. Kunz and R. J. Luebbers, *The Finite Difference Time Domain Method for Electromagnetics*, CRC press, 1993.
- [35] F. Hunsberger, R. Luebbers, and K. Kunz, "Finite-difference time-domain analysis of gyrotropic media. I. Magnetized plasma," *IEEE Trans. Antennas Propag.*, vol. 40, no. 12, pp. 1489-1495, 1992.
- [36] F. P. Hunsberger, Jr., "Extension of the finite-difference time-domain method to gyrotropic media," 1991.
- [37] J. Zhang, X. Yuan, C. Wang, and Y. He, "Comparative analysis of two-coil and three-coil structures for wireless power transfer," *IEEE Trans. Power Electron.*, vol. 32, no. 1, pp. 341-352, 2017.
- [38] IEEE Standards Coordinating Committee 28, *IEEE Standard for Safety Levels with Respect to Human Exposure to Radio Frequency Electromagnetic Fields, 3kHz to 300 GHz*, Institute of Electrical and Electronics Engineers, Incorporated, 1992.
- [39] P. Kosta, *et al.*, "Electromagnetic safety assessment of a cortical implant for vision restoration," *IEEE J. Electromagn. RF Microw. Med. Biol.*, vol. 2, no. 1, pp. 56-63, 2018.
- [40] S. Pokhrel, M. Rodriguez, A. Samimi, G. Heber, and J. Simpson, "Parallel I/O for 3-D global FDTD earth-ionosphere waveguide models at resolutions on the order of ~ 1 km and higher using HDF5," *IEEE Trans. Antennas Propag.*, 2018.